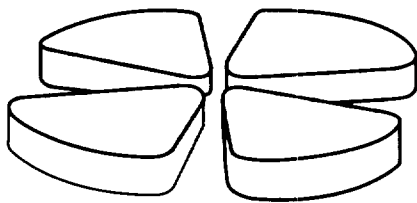# GANIL

Experimental Determination of Fragment Excitation Energies

in Multifragmentation Events.*

N. Marie[1], A. Chbihi[2], J.B. Natowitz[1], A. Le Fèvre[2], S. Salou[2], J.P. Wieleczko[2],

L. Gingras[2], M. Assenard[3], G. Auger[2], Ch.O. Bacri[4], F. Bocage[5] B. Borderie[4],

R. Bougault[5], R. Brou[5], P. Buchet[6], J.L. Charvet[6], J. Cibor[1], J. Colin[5], D. Cussol[5],

R. Dayras[6], A. Demeyer[7], D. Doré[6], D. Durand[5], P. Eudes[3], J.D. Frankland[4], E. Galichet[7],

E. Genouin-Duhamel[5], E. Gerlic[7], M. Germain[3], D. Gourio[10], D. Guinet[7], K. Hagel[1],

P. Lautesse[7], J.L. Laville[2], J.F. Lecolley[5], T. Lefort[5], R. Legrain[6], N. Le Neindre[5],

O. Lopez[5], M. Louvel[5], Z. Majka[1], A.M. Maskay[7], L. Nalpas[6], A.D. Nguyen[5], M. Parlog[8],

J. Péter[5], E. Plagnol[4], A. Rahmani[3], T. Reposeur[3], M.F. Rivet[4] E. Rosato[9],

F. Saint-Laurent[2], J.C. Steckmeyer[5], M. Stern[7], G. Tabacaru[8], B. Tamain[5], O. Tirel[2],

E. Vient[5], C. Volant[6] R. Wada[1].

GANIL P 98 13

Experimental Determination of Fragment Excitation Energies

in Multifragmentation Events.[*]

N. Marie[1], A. Chbihi[2], J.B. Natowitz[1], A. Le Fèvre[2], S. Salou[2], J.P. Wieleczko[2],

L. Gingras[2], M. Assenard[3], G. Auger[2], Ch.O. Bacri[4], F. Bocage[5] B. Borderie[4],

R. Bougault[5], R. Brou[5], P. Buchet[6], J.L. Charvet[6], J. Cibor[1], J. Colin[5], D. Cussol[5],

R. Dayras[6], A. Demeyer[7], D. Doré[6], D. Durand[5], P. Eudes[3], J.D. Frankland[4], E. Galichet[7],

E. Genouin-Duhamel[5], E. Gerlic[7], M. Germain[3], D. Gourio[10], D. Guinet[7], K. Hagel[1],

P. Lautesse[7], J.L. Laville[2], J.F. Lecolley[5], T. Lefort[5], R. Legrain[6], N. Le Neindre[5],

O. Lopez[5], M. Louvel[5], Z. Majka[1], A.M. Maskay[7], L. Nalpas[6], A.D. Nguyen[5], M. Parlog[8],

J. Péter[5], E. Plagnol[4], A. Rahmani[3], T. Reposeur[3], M.F. Rivet[4] E. Rosato[9],

F. Saint-Laurent[2], J.C. Steckmeyer[5], M. Stern[7], G. Tabacaru[8], B. Tamain[5], O. Tirel[2],

E. Vient[5], C. Volant[6] R. Wada[1].

[1] *Cyclotron Institute, Texas A & M University, College Station, Texas 77843-3366.*

[2] *GANIL, CEA, IN2P3-CNRS, B.P. 5027, F-14021 Caen Cedex, France.*

[3] *SUBATECH, Université de NANTES, École des Mines de NANTES, IN2P3-CNRS, F-44072*

Nantes Cedex 03, France.

[4] *Institut de Physique Nucléaire, IN2P3-CNRS, F-91406 Orsay Cedex, France.*

[5] *LPC, IN2P3-CNRS, ISMRA et Université, F-14050 Caen Cedex, France.*

[6] *DAPNIA/SPhN, CEA/Saclay, F-91191 Gif sur Yvette Cedex, France.*

[7] *IPN Lyon, IN2P3-CNRS et Université, F-69622 Villeurbanne Cedex, France.*

[8] *National Institute for Physics and Nuclear Engineering, RO-76900 Bucharest-Măgurele,*

Romania.

[9] *Dipartimento di Scienze Fisiche, Univ. di Napoli, 180126 Napoli, Italy.*

[10] *Gesellschaft für Schwerionenforschung, D-64291 Darmstadt, Germany.*

1

Abstract

For 50 MeV/nucleon ^{129}Xe + ^{nat}Sn multifragmentation events, we deduced, by means of correlation techniques, the multiplicities of the hydrogen and helium isotopes which were emitted by the hot primary excited fragments produced at the stage of the disassembly of an equilibrated hot source. We also derived the relative kinetic energy distributions between the primary clusters and the light charged particles that they evaporate. From the comparison between the secondary multiplicities observed experimentally and the multiplicities predicted by the GEMINI model, we concluded that the source breaks into primary fragments which are characterized by the same N/Z ratio as the combined system. Knowing the secondary light charged particle multiplicities and kinetic energies, we reconstructed the average charges of the hot fragments and we estimated their mean excitation energies. The fragment excitation energies are equal to 3.0 MeV/nucleon for the full range of intermediate mass fragment atomic number. This global constancy indicates that, on the average, thermodynamical equilibrium was achieved at the disassembly stage of the source.

25.70Pq

I. INTRODUCTION

In several recent publications, analyses of many features of multifragmentation events occurring in the central collisions of ^{129}Xe + ^{nat}Sn at 50 MeV/nucleon have been presented [1-4]. Analyses of both light charged particle (Z ≤ 2) and fragment (Z ≥ 3) data indicate that the mechanism is one of disassembly of a single equilibrated source formed in those collisions. Comparisons of the experimental data to Statistical Multifragmentation Model (SMM) [5-7], Expanding Emitting Source (EES) [8] and Boltzmann Nordheim Vlasov (BNV) [9] calculations have shown that the kinetic energies of light charged particles and fragments can essentially be understood as reflecting the multiple emission steps occurring during different phases of the disintegration of the system. In the framework of these models, the scenario for the multifragmentation process which emerges is one in which the compressed equilibrated hot source first expands, emitting mainly light particles. When the system reaches a sufficiently low density, intermediate mass fragments (IMF) may be abundantly produced, either through a freezing out process [5] or through rapid sequential emission [8]. Lighter charged species may also be emitted in this phase. The primary fragments may be excited and if so, are expected to decay by normal statistical processes. A direct observation of this secondary statistical component and extraction of the excitation energies and sizes of the primary fragments can provide a very significant test of the models and of the assumption of thermodynamical equilibrium at the time of disassembly.

In this paper, we present the results of an experimental analysis of the 50 MeV/nucleon ^{129}Xe + ^{nat}Sn multifragmentation events in which light charged particle-IMF correlations have been employed to determine the average multiplicities of particles emitted from de-exciting primary fragments. From these data, both the average excitation energies and the masses of the primary fragments have been derived. These results indicate that the fragments are formed with the same N/Z ratio as the initial system ^{129}Xe + ^{nat}Sn and that their excitation energies per nucleon are all the same. This provides strong evidence that,

3

on the average, thermodynamical equilibrium is achieved when the primary fragments are produced.

II. EXPERIMENTAL PROCEDURES

A. Event selection

The 50 MeV/nucleon ^{129}Xe + ^{nat}Sn events analysed in this paper were obtained during an experiment performed at the GANIL facility. The charged products of these events were detected with the multidetector INDRA [10–12]. In references [1–3], the multifragmentation events originating from very central collisions of 50 MeV/nucleon ^{129}Xe + ^{nat}Sn were isolated by requiring events for which the total detected charge exceeds 80 % of the total charge of Xe+Sn system and for which the flow angle $\theta_f \geq 60^o$. The flow angle, θ_f, is the angle between the beam axis and the principal axis associated with the ellipsoid which approximates the kinetic energy event shape [13]. From the analysis made on this event sample, it was concluded that in such collisions, an isotropically disintegrating equilibrated source is formed [1]. Its initial charge represents 86 % of the total charge available. The remaining charge is accounted for a small number of light charged particles which are strongly forward/backward focused in the center of mass [1]. The total mean multiplicity of light charged particles per event is 27.5 and the mean multiplicity of IMF per event is 7.1. The domain of the IMF atomic number ranges from $Z_{IMF}=3$ to $Z_{IMF}=30$. Application of the calorimetric method on the isotropically emitted species gives a mean excitation energy of the source of 12 ± 0.5 MeV/nucleon. The kinetic energies of the fragments are interpreted as reflecting expansion effects which lead to a measured collective energy of about 2 MeV/nucleon at the freezeout time. Calculations using the EES model suggest that the light charged particle kinetic energies may be reproduced by taking into account the time evolution of the system [2]. For more details, see references [1–3].

For this work, the event selection criteria are very similar to those used in the earlier

4

work. However, since application of the decorrelation technique requires good statistics, we have chosen to treat experimental events characterized by $\theta_f \geq 45^\circ$. The widening of the selection might lead to a slight pollution from binary events but it has been verified that this new event sample has the same global features as the previous one, selected with a $\theta_f \geq 60^\circ$. This fact is illustrated in Table I and Table II. Table I shows the average multiplicities of light charged particles, intermediate mass fragments and fragments of various atomic numbers accounted for the isotropic source, for events characterized by $45^\circ \leq \theta_f \leq 60^\circ$ (left column), and for events characterized by $\theta_f \geq 60^\circ$ (right column). Table II shows the average kinetic energies of Z=1 and Z=2 isotopes, Li, Ne and S fragments associated to the isotropic source, for the two different selections in flow angle. The numbers in brackets represent the statistical errors, i.e $\sigma/\sqrt{N}$, where N is the number of particles considered. We have made no special requirement for the angular domain at which the light charged particles are detected as the correlation functions have equivalent forms whether or not we limit the angular domain for the light charged particle emission.

B. Particle emission sources

In dealing with complex multifragmentation events, the first question to be addressed is whether a distinct secondary statistical component can be observed in the presence of the other particles emitted. To answer this question, we first calculated event by event, for each detected IMF, the relative velocities between that IMF and all light charged particles in an event. We then determined the projections of these relative velocities onto the axis representing the IMF direction in the center of mass frame and into a plane perpendicular to that axis. The components of these projections are designated by $V_{\parallel}^{IMF}$ and V_{t}^{IMF}. This treatment allows us to define a common system of reference for an ensemble of fragments that have different directions in the center of mass. In figure 1, we present examples of $V_{\parallel}^{IMF}$ - V_{t}^{IMF} diagrams obtained for alpha particles detected in coincidence with B, Ne, P

5

and Ca fragments. The overall pattern observed is one of near isotropic emission centered at $V_{\parallel}^{IMF}$ values in the -3 to -4 cm/ns range. The mean IMF velocities in the center of mass are in the 2 - 4 cm/ns range. Thus the dominant emission observed is essentially isotropic in the center of mass frame. However, we also clearly observe circles which are centered at the IMF velocities and with radii which increase with the detected fragment atomic number. Such circles are observed for all hydrogen and helium isotopes, and with IMF of other atomic numbers. By the means of simulations and a decorrelation technique (described below), we verified that this effect is not related to the INDRA geometry and we conclude that these circles clearly reflect the Coulomb repulsion between light charged particles and intermediate mass fragments.

In order to further explore whether some of these light charged particles originate from the de-excitation of the primary fragments, which are the parents of the detected IMF, we then constructed relative velocity spectra between light charged particles and IMFs. In figure 2, the resultant spectra are presented for alpha particles detected in coincidence with Neon and for protons detected in coincidence with Sulphur respectively. The experimental data are represented by continuous histograms. If the detected fragments are residues from primary fragments, their average velocities are expected to be the same as the average velocities of the initial parents. Therefore, particles evaporated from the IMF parent would be expected to appear at small relative velocities corresponding to emission at near Coulomb barrier energies. The fact that an excess of particles which might be expected at such low relative velocities is not clearly visible in figure 2, indicates that the evaporated component represents a relatively small contribution to the whole spectrum. These secondary particles are difficult to observe given the apparently large amount of light charged particles produced in other phases of the source disintegration. Therefore, to observe and extract them, it is necessary to have a reference spectrum in which such secondary particles do not make a large contribution or in which their correlation with the IMFs is negligible. This suggests use of a decorrelation technique such as that used in particle-particle correlation measurements.

Such a method has already revealed itself as very powerful [14].

III. DECORRELATION TECHNIQUE

For two particle correlations, the basic idea of decorrelation techniques is to compare an observable constructed with couples of particles, detected in coincidence in the same correlated event, to the same observable built with couples formed by replacing one of the two particles by a like particle, produced in a different event, and therefore totally independent of the first one. Ideally, in these uncorrelated events, the correlations that existed in the correlated events should be destroyed. The spectra of the observables obtained with the two different samples of couples may then be compared to isolate differences reflecting real physical effects. In general, the spectra are compared by dividing the correlated distribution by the uncorrelated one. The resulting spectrum is then designated as the correlation function which is symbolised by this expression :

$$R = N \frac{P_{A_i,B_i}}{P_{A_i,B_j}} \tag{1}$$

where P_{A_i,B_i} is the number of correlated pairs of particles A and B detected in the same event i, P_{A_i,B_j} is the number of uncorrelated pairs formed by particles produced in two different events i and j, and N is a normalization factor. This factor is often defined by making the distributions superimposable in a region where the sought after physical effect is not expected.

Decorrelating fragments and particles in multiparticle events presents some particular difficulties which must be overcome. For such complex events, with many fragments, the interactions between all particles and not just those between a particle pair can be important. Decorrelating a particular pair may then result in the loss of other pairwise correlations which should in fact be preserved in order to define a correct background spectrum.

A. Development of decorrelation procedures

In order to test various decorrelation procedures for multiple fragment events, we have used simulations which were performed with a modified version of the phenomenological event generator SIMON [15]. Simulated events were calculated with input parameters which reasonably reproduce the experimental observed kinematical characteristics of the fragments and light charged particles [3]. In this generator, the calculation of the trajectories of all the reaction products is performed by taking into account the Coulomb interactions at each step of the source disintegration. An important feature of the modified generator is its ability to treat the light charged particle emission occurring before the formation of the primary fragments, separately from the secondary evaporation resulting from the deexcitation of the primary fragments. Indeed, these two different emission phases may contribute to the total relative velocity spectrum. In figure 3(a), the solid histogram represents the total spectrum of relative velocities for protons emitted in coincidence with Ne. The distinct contributions from each phase are also illustrated. The dot-dashed histogram represents the spectrum of protons emitted during the first step of the system de-excitation, before disassembly into fragments. We call this spectrum the primary emission spectrum. The dashed and hatched histogram represents the spectrum of protons evaporated by the primary excited fragments which produce the detected Ne isotopes. This spectrum is hereafter designated as the secondary evaporated spectrum. This is the component analogous to that which we wish to extract from the experimental data. The dotted histogram corresponds to the secondary evaporation of protons from all the other primary fragments, i.e. those which do not decay into Ne. To decorrelate events, we tried a number of different procedures based on two particle decorrelation techniques. While each of these allowed us to see the effect we were attempting to explore, most were not satisfactory as residual correlations among other particles in the same event led to shifts in the background distribution which would only be removed by rather subjective techniques. For this reason, we finally settled on a decorrelation technique based on Li containing events.

8

In using the simulations to construct relative velocity spectra for particles in coincidence with each detected IMF, we noted that the calculation predicts that the relative contribution of the secondary evaporated spectrum associated with Li is very weak as compared to that for heavier fragments. This effect is shown figure 3(b) where the spectrum of particles emitted by Li parents is symbolized by the hatched area. The primary component (dot-dashed histogram) and the secondary contribution from the other primary fragments (dotted histogram) are also presented for these Li containing events. The explanation for the low multiplicity of the secondary component is that, in the simulated events, 20 % of the Li are primary fragments which decay only through neutron emission and 72 % of the Li are the residues from the disintegration of small primary fragments, lighter than Silicon fragments. We have taken advantage of the fact that very few light charged particles are emitted by the parents of Li in our attempts to construct the decorrelated spectra which we use in this work. Specifically, we follow a procedure in which : for every event where a Li is produced, we replace the velocity modulus of the Li by the velocity modulus of a heavier fragment, taken from another event. At the same time, the chosen IMF is given the original direction of the Li fragment. We have checked that events containing at least one Li represent 80 % of the event sample. Since Li isotopes are correlated with very few light charged particles, this technique allows us to mimic an event where the parent of the chosen IMF would have emitted almost no light charged particles and the secondary emission is from other primary fragments in the event. We then construct the relative velocity spectrum between this virtual fragment and the light charged particles. We then normalize the decorrelated spectrum to the correlated spectrum using the ratio between the production rate of the chosen IMF and the production rate of Li. In this way, both the correlated and uncorrelated spectra correspond to the same total number of fragments.

For simulated events, the decorrelated spectrum constructed for Ne with the technique described above is presented in figure 3(b) (continuous histogram). The spectral shapes are quite similar. In order to compare the two relative velocity spectra in detail, we have

9

calculated both the ratio of the two, the correlation function designated by R, and their difference, the difference function symbolised by Δ, as a function of relative velocity. For the simulated events, these are shown in figure 3(c) and figure 3(d) respectively. Since in the calculations we know the origin of each particle, we have hatched the area on each plot corresponding to the secondary emission from the parents of the Ne fragments. We note in this treatment that the background of the difference function is negative and therefore its equivalent is located below the R=1 line in the correlation function. This feature can be understood by looking at the differences between the correlated and uncorrelated contributions, for example in figure 3(a) and figure 3(b). The amplitude of the primary component is the same for both correlated and uncorrelated events, but the intensity of the secondary emission from the other primary fragments is higher for Li containing events than for events selected by requiring heavier fragments. For background events, alone this difference in amplitude therefore would result in a difference function which is negative (figure 3(d)) and in a correlation function which is less than 1 (figure 3(c)).

The results of the simulation suggest a procedure to decorrelate events that can enable us to observe, in the experimental relative velocity spectra, the component originating from the secondary decay of primary fragments formed in multifragmentation events. They also indicate that, in order to extract the spectrum of evaporated particles, we need to determine the shape of the background in the correlation function. Once again, the simulations have proved to be a very useful guide for this task.

In the generated events, we can determine the background by omitting from the correlated spectrum the secondary evaporated contribution from the parents of the IMF being considered, and, applying the subtraction and division operations to the residual correlated and uncorrelated spectra. The backgrounds determined with this method are shown in figure 3(c) and figure 3(d) as dashed histograms. For the correlation and difference functions, they are respectively very similar to a hyperbola or to a gaussian.

10

By fitting the backgrounds obtained for correlation functions such as those in figure 3(c), we found that the background shape is well fitted by the equation

$$R(V_{rel}) = 1.2 - \frac{1}{aV_{rel} + b} \tag{2}$$

where V_{rel} designates the relative velocity, and a and b are two parameters which differ for each IMF. Since in the experimental data we do not have a means of directly observing the background, we assume in the following analysis that the experimental background has the same general shape, and attempt to define the parameters a and b from the experimentally determined correlation and difference functions. These parameters can be calculated by solving the equation (2) for two different points at which the secondary evaporated spectrum leading to the selected IMFs can be neglected. We use both functions R and Δ to select those points. In the simulations, we have observed that the secondary evaporation disappears at the first minimum in the difference function, at V_{1rel}, and again after the second minimum, at V_{2rel}, the first point at which $\Delta = 0$. Having found the relative velocities associated with these two points, V_{1rel} and V_{2rel} , we can determine in the correlation function their associated R_1 and R_2 ordinates. With the points (V_{1rel}, R_1) and (V_{2rel}, R_2), the a and b parameters in equation (2) are deduced and then, the function reflecting the background is determined. From this background defined for the correlation function, we can derive the corresponding background in the difference function.

In figure 3(e) and figure 3(f), we present the backgrounds deduced from the procedure described (dashed histograms). A comparison with the real backgrounds, presented in figure 3(c) and figure 3(d), shows they are generally well reproduced. Subtracting the backgrounds in figure 3(e) and figure 3(f) from the respective functions, we recover 91 % of the actual secondary emission spectra associated with the Ne parents, and for the ensemble of produced prefragments, we recover on average 84 % of the protons they evaporated. This gives us some confidence that the same techniques may be applied to the experimental data. We note that the same background shape has been used for all particles.

B. Application to experimental events

We applied the procedure described above to the experimental data for each IMF and for each hydrogen and helium isotope. The correlated spectra which are obtained for alphas in coincidence with Neon fragments and protons in coincidence with Sulphur fragments are compared to the corresponding uncorrelated spectra in figure 2 (dashed histograms). In figures 4(a) to 4(f), 5(a) to 5(d) and in figures 4(g) to 4(l), 5(e) to 5(h) we present examples of the difference functions and the correlation functions associated with hydrogen and helium isotopes correlated with fragments of various sizes. In the case of ^{3}H and ^{3}He, multiplicities are low. Therefore, it was necessary to add spectra for several Z_{IMF} in order to be able to observe distinctly the evaporated peak. We have derived the backgrounds of the correlation and difference functions for Z=1 and Z=2 isotopes and each detected Z_{IMF}. Examples of the derived backgrounds are presented in figures 4(a) to 4(f), 5(a) to 5(d) and in figures 4(g) to 5(l), 5(e) to 5(h) as dashed lines. For the experimental data, there are larger fluctuations in the difference functions than observed for the simulations. These fluctuations in some cases appear larger than statistical. We have considered the possibility of well defined resonance states but have not been able to definitely identify these fluctuations as resulting from such states. This introduces some uncertainty in the definition of the background.

The difference between the difference function and its associated background gives directly the IMF associated component that we are interested in. The resulting secondary evaporated spectra are presented figures 4(m) to 4(r) and 5(i) to 5(l). If we consider the detected fragments as residues, those spectra are those of the evaporated light charged particles emitted during the decay of the primary parent fragments. In some spectra, we observe negative dips which correspond to the region in the correlation and difference functions where the background goes through fluctuations at large relative velocities. This results from the fact that the background has been optimized for the region of the evaporation peak. Therefore, for the following analysis, we will consider only the positive part of the secondary evaporated spectra in the velocity range between the first minimum of the differ-

ence function and the velocities designated by the arrows drawn in figures 4 and 5.

In summary, with the aid of an event simulator, we have developed a technique to approximate the background shape in our experimental light charged particle-IMF correlation functions. By applying this procedure to the 50 MeV/nucleon $^{129}Xe+^{nat}Sn$ multifragmentation events, we can extract the velocity spectra of secondary particles emitted by the hot fragments produced during the disassembly of the excited source.

It is interesting to ask whether some light IMFs also result from secondary emission processes. In order to answer this question, we constructed the correlation functions between Li and larger fragments. For this case, in a manner similar to that used for Li events in the previous section, the Be velocities were replaced by those of heavier IMFs and, correlation and difference functions analogous to those for lighter particles were constructed. We did not observe peaks in either the difference or in the decorrelation functions. Therefore, in the framework of the decorrelation procedure we have developed, we conclude that the de-excitation of primary excited fragments which leads to a Li and a larger IMF is a rare process in the events under study.

IV. RECONSTRUCTION OF THE PRIMARY FRAGMENT CHARACTERISTICS

A. Secondary light charged particle multiplicities

From the secondary emission spectra, it is possible to extract physical quantities that will enable us to reconstruct the average characteristics of the primary fragments, i.e. their sizes and excitation energies. If each fragment is considered as a residue of the de-excitation of a primary fragment, the number of particles in the secondary evaporated spectra gives directly the average number of helium and hydrogen isotopes emitted in the decay of the

13

primary excited fragments. From these, knowing the production rate for IMF of each atomic number, we can deduce the average evaporated light charged particle multiplicities per IMF. These multiplicities are shown figure 6 as a function of the IMF atomic number, for $Z=1$ and $Z=2$ isotopes detected in coincidence with fragments of atomic number in the range of $4 \leq Z_{IMF} \leq 20$. Above $Z_{IMF}=20$, the statistics were insufficient to extract reliable quantities. The error bars represent the estimated uncertainty in the mean value, resulting from the uncertainties in the background reconstruction due to the presence of fluctuations (refer to paragraph III.B). They are the largest deviations seen using three different techniques for determining the two points at which the backgrounds in the correlation and difference functions are normalized.

In figure 6, we see that the light charged particle multiplicities increase with increasing Z_{IMF}. Such an increase suggests increasing total excitation energy of the parent fragments. Multiplicities of protons, deuterons and alphas are comparable. Triton and ^{3}He multiplicities are significantly lower and show less variation with Z_{IMF}.

From these data, it is possible to determine the fraction of the light charged particle multiplicity associated to the isotropic source, which can be accounted for by secondary particle evaporation from the primary fragments. For this purpose, we have first made a linear extrapolation of the secondary multiplicities per IMF in order to estimate those corresponding to fragments with atomic numbers greater than 20. Then, from the known production rate of IMF, we have deduced the average secondary multiplicity per event, M_s, for the $Z=1$ and $Z=2$ isotopes. These are shown in the second column of Table III. The superscripted and subscripted numbers represent the absolute uncertainties and the corresponding percentage uncertainties. The average multiplicities per event of light charged particles emitted by the isotropic source, M_{iso}, are presented in the third column. The percentages, P, of the secondary evaporated particles with respect to the isotropic component, and their associated absolute uncertainties are given in the last column. The comparison between M_{iso} and M_{tot} shows that, on average 27.9 ± 5 % of the particles emitted isotropically by the excited source originate from the cooling of the primary fragments. Since the heaviest fragments

14

have the smallest production rate, without the extrapolation for fragments with atomic numbers greater than 20, this percentage is very similar and equal to 26.2 ± 5 %. This may be slightly underestimated as it was shown in section III.A that only 84 % of protons emitted from fragments in the simulation were recovered by the method used. The other particles must then be emitted earlier, either while the source expands or during the disassembly of the source into fragments [8]. The percentage of secondary ^{3}He is very high in comparison with the percentages observed for the other light particles. We will discuss this point in paragraph IV.C.

B. Secondary light charged particle kinetic energies

From the relative velocity spectra, we can also determine the kinetic energy distributions of the evaporated light charged particles. The relative kinetic energies are calculated using the formula : $E_{rel} = 0.5 \ A \ V^2_{rel}$, where A designates the mass of the Z=1 or Z=2 isotope which is considered. The resulting mean relative kinetic energies of the hydrogen and helium isotopes are presented figure 7 as a function of the detected fragment atomic number. We note that for each isotope, the relative kinetic energies vary only slightly over the fragment atomic number range from Z_{IMF}=4 to Z_{IMF}=20. We have fitted the relative kinetic energy spectra by a maxwellian distribution for surface emission :

$$P(E_{rel}) \alpha \frac{E_{rel} - E_B}{T^2} e^{-(\frac{E_{rel} - E_B}{T})} \tag{3}$$

In this formula, T designates the apparent temperature of the source and E_B is the Coulomb barrier. We performed the fit on the relative kinetic energy spectra of the different hydrogen and helium isotopes, for each detected IMF. The resulting parameters E_B and T are presented in figure 8 and figure 9 respectively, as a function of the IMF atomic number. We observed that the Coulomb barrier, E_B, increases slightly with the atomic number of the fragment. The mean value of the apparent temperatures calculated for the fragments whose atomic number is in the range $4 \leq Z_{IMF} \leq 20$, is symbolized by the dotted lines. For each

15

particle type, the apparent temperatures fluctuate about a constant value over the whole range of detected fragment atomic number but the mean apparent temperatures differ significantly between the different hydrogen and helium isotopes. This last fact is worrisome and we could not find a satisfactory explanation for it. These differences seem larger than those expected from time effects in the de-excitation of the primary fragments and they do not appear in the GEMINI calculations (refer to paragraph V.B). However, it appears most likely that the differences reflect uncertainties in the background shape approximation. Indeed, this background shape has been derived from the background predicted for protons in the simulations. Alternatively, Coulomb effects from other species produced in these complex events might also explain the differences in the mean temperatures observed (see section V.B.). The mean temperature obtained for ^{3}He is very high relative to the others. We will discuss about this in paragraph IV.C.

C. Multiplicity determinations for ^{3}He

The total multiplicity for ^{3}He emission is very low, as seen in Table III. In contrast, we note that the secondary multiplicity (Table III, paragraph IV.A.) and apparent temperature of the kinetic energy spectra (figure 9, paragraph IV.B) obtained for ^{3}He are significantly larger than the ones observed for the other hydrogen and helium isotopes.

A possible reason is that, for ^{3}He, the procedure that we developed in order to construct the correlation functions and approximate the background shapes may be inadequate. Indeed the experimental ^{3}He spectra are strongly different from those of ^{4}He, exhibiting a larger average energy [1]. The very low ^{3}He multiplicity makes the absolute determination very sensitive to background uncertainties. Therefore, for this species, using this technique, we may extract not only particles emitted by the excited primary fragments, but we may pick up also some ^{3}He which were produced before the disassembly of the source into fragments, or during disassembly.

However, we see in figure 5, well defined peaks which argue strongly for ^{3}He emission and

16

note that these appear significantly broader than the ^{4}He secondary emission peaks. This suggest that part of the secondary ^{3}He multiplicity that we extracted might originate from the decay of particle unstable states of complex nuclei. Likely candidates for such emission are the E*=16.66 MeV state of ^{5}Li which decays into ^{3}He-d, the E*=21.0 MeV state of ^{6}Li which decays into ^{3}He-t, the E*=17.0 MeV state of ^{7}Be which decay into ^{3}He-^{4}He or the E*=19.29 MeV state of ^{10}Be which decay in ^{3}He-^{4}He-n [16]. For the events under study, the existence of such states would explain also the large width of the relative velocity spectra observed for the ^{3}He (figure 5, paragraph III.B). We attempted to verify this hypothesis by the study of the ^{3}He-^{4}He, ^{3}He-d and ^{3}He-t correlations for the multifragmentation event sample we use for this analysis. Neither in the difference functions nor in the correlation functions were we able to observe peaks which would indicate significant contributions from such states, although we could observe the ^{8}Be and ^{6}Li resonances in the ^{4}He-^{4}He and ^{4}He-d correlation functions. Therefore, we believe that the most likely reason for the large ^{3}He secondary multiplicities and apparent temperatures is the uncertainty in the definition of the background which leads to particularly large uncertainties for very low multiplicity particles.

D. Atomic numbers and masses of the primary fragments

From the average secondary multiplicities presented figure 6, it is possible to estimate the average atomic numbers $<Z_{pr}>$ of the primary fragments. This average primary fragment atomic number is determined by adding to the detected fragment atomic number Z_{IMF}, the evaporated light particle atomic numbers weighted by their associated multiplicities $<M>$.

$$< Z_{pr} >= < Z_{IMF} > + < M_{^1H} > + < M_{^2H} >$$
$$+ < M_{^3H} > + 2(< M_{^3He} > + < M_{^4He} >) \qquad (4)$$

For this purpose, we estimated the average ^{3}H and ^{3}He secondary multiplicities corresponding to each detected fragment from the values obtained by adding spectra for several IMF (refer above).

17

In order to estimate the primary fragment masses, we have initially made two assumptions. In the first, we assumed that the prefragments were in the valley of stability with masses A_{pr} which are calculated with the following formula :

$$A_{pr} = 1.867 Z_{pr} + 0.016 Z_{pr}^2 - 1.0710^{-4} Z_{pr}^3 \qquad (5)$$

This expression approximates the valley of stability [17]. It has been used to assign average masses A_{IMF} to the detected IMFs in order to calculate their velocities. Alternatively, we have assumed that the final fragments are in the valley of stability but that the primary fragments have the same N/Z ratio as the disassembling system which, in turn, is expected to be essentially that of the ^{129}Xe$+^{nat}$Sn combined system, i.e. N/Z=1.38. In this case A_{pr} is given by :

$$A_{pr} = Z_{pr} + 1.38 Z_{pr} \qquad (6)$$

The values of, Z_{pr} and the two different estimates of A_{pr} are shown in figures 10(a) and 10(b) as a function of the detected fragment atomic number and mass.

For the two different assumptions regarding parent N/Z ratio, the excitation energies of the primary fragments can be estimated by summing the total kinetic energies of all particles emitted and the Q value for the emission process.

$$E^* = \sum_i M_i E_i + M_n E_n + Q \qquad (7)$$

Here M_i are the average multiplicities of the hydrogen and helium isotopes emitted by the hot fragments. They are those presented in figure 6. E_i are the average relative kinetic energies of the Z=1 and Z=2 isotopes shown in figure 7. M_n is the number of neutrons produced in the course of the disintegration cascade. M_n is deduced from the difference between the mass A_{pr} of the primary fragment and the total detected mass A_{det} which is the sum of the detected charged particle masses, including the residue :

$$< A_{det} > = < A_{IMF} > + < M_{^1H} > + 2 < M_{^2H} > +$$

$$3 < M_{^3H} > + 3 < M_{^3He} > + 4 < M_{^4He} > \qquad (8)$$

18

E_n is the kinetic energy of a neutron in the system of reference of the emitter nucleus. It is estimated from the relative kinetic energy E_{1H} of the proton, from which we deduct the Coulomb barrier energy. This last energy was calculated with the formula of [18]. Q is the mass difference between the primary fragment and the final products. The Q values were calculated using the liquid drop formula proposed by Seeger and Prisho [19].

Figure 11 shows the average excitation energies estimated with the above method, as a function of the primary fragment atomic number Z_{pr}. Figure 11(b) corresponds to the case where the masses A_{pr} of the initial fragments are assumed to be in the valley of stability, and figure 11(a) corresponds to the case where the parent fragments are assumed to have the same N/Z ratio as the combined system. The values deduced from the two distinct assumptions differ significantly. This difference is due to the fact that the number of neutrons that we estimate for this reconstruction is very different for the two different assumptions regarding N/Z ratio in the parent. In both cases the excitation energies of the initial fragments increase almost linearly with the fragment atomic number. When we assume that the fragments belong to the valley of stability, the linear increase indicates a mean excitation energy per nucleon of 1.6 MeV/nucleon. On the contrary, when we suppose that they conserve the N/Z ratio of the initial system, their mean excitation energy per nucleon is 3.0 MeV/nucleon. Moreover, the excitation energy per nucleon deduced for each prefragment varies very little around this mean value. This result indicates that, on the average, thermodynamical equilibrium was achieved at the moment of the breakup of the source into excited fragments, and it reinforces the similar conclusion of equilibration that was derived earlier from the comparison of the experimental multiple fragment production events with the predictions of the Statistical Multifragmentation Model [2]. It should be noted that the excitation energy of the multifragmenting source at the moment of the prefragment formation is larger than the prefragment excitation energies. In order to evaluate it, we should add to the excitation energies and kinetic energies of the hot primary fragments, the kinetic energies of the light charged particles which are also produced at this disassembly stage. Moreover, we would need to know their multiplicities and the size of the source at this time

in order to calculate the Q value of the reaction which enters also in the source excitation energy calculation. All these quantities are unknown and can not be extracted from the information that we possess without the use of models which describe well the scenario of multifragmentation on which our analysis relies.

At this point, it is reasonable to ask whether the mean excitation energy derived from the experimental data is very sentitive to the procedures we use to evaluate it. In order to explore the sensitivity, we performed simulations in which the prefragments have a much higher excitation energy of 7.5 MeV/nucleon. We find that the fraction of protons recovered is rather insensitive to the assumed excitation, i.e. 84 % at 4.3 MeV/nucleon excitation and 81 % at 7.5 MeV/nucleon excitation. Given this result, it does not appear that the experimentally reconstructed excitation energy is limited by the reconstruction techniques.

V. COMPARISON WITH THE GEMINI CALCULATION

In an attempt to distinguish between the two different assumptions regarding primary fragment N/Z ratio, we have compared the experimental results to the predictions of the statistical model code GEMINI [20]. For this purpose, we simulated separately the de-excitation of a set of excited compound nuclei having atomic numbers, Z_{pr}, equal to those determined experimentally for the primary fragments, and masses equal either to those deduced from the valley of stability assumption, or those corresponding to the values estimated assuming conservation of the entrance channel N/Z ratio. In the valley of stability case, we performed two calculations for which the excitation energies were fixed at 1.5 and 2 MeV/nucleon. For the N/Z ratio conservation case, excitation energies of 2.5 or 3. MeV/nucleon were used. These choices are based on the estimates obtained from the method described paragraph IV D. In figure 11 we compare, for the two different assumptions on reconstruction of A_{pr}, the total excitation energies of the primary fragments obtained from the experimental data (black circles) to those calculated for the simulations (open symbols).

20

A. Secondary light charged particle multiplicities

In figure 12, we compare the multiplicities of neutrons and light particles predicted by GEMINI to the experimentally observed multiplicities of hydrogen and helium isotopes (black circles) and to the neutron multiplicities estimated when we assume that the primary fragments conserve the N/Z ratio of the entrance channel (black triangles). For this purpose, the Z_{IMF} from the calculation corresponds to the mean value of the atomic number distribution, resulting from an event by event selection, of the biggest fragment left after the de-excitation of the assumed primary fragment. For the data, they are the detected fragment atomic numbers. When we assume that the primary fragments are neutron rich (entrance channel N/Z ratio) and that they have excitation energies of 2.5 to 3 MeV/nucleon (open symbols), the results of the calculation are in generally good agreement with the experimental data for all but ^{3}He, although the calculated ^{1}H multiplicities are somewhat larger than the experimental values for the heaviest fragments. As noted, the ^{3}He experimental multiplicities are much larger than the predicted ones, for the whole range of primary fragment atomic number.

For the energy reconstruction, we have assumed that the detected fragments, which we consider to be residues of the primary fragments, are in the valley of stability. For the neutron rich parents in the model calculation, we noted that the average N/Z ratios of the biggest fragments remaining after the cooling of the compound nuclei, and which we consider as residues, are in the range of 1.1 to 1.2 for fragments lighter than Z=15, and for heavier fragments, the ratios correspond to the valley of stability line.

For the simulations obtained with the assumption that the primary fragment masses belong to the valley of stability and that the initial excitation energies are equal to 1.5 or 2 MeV/nucleon (lines), we observe a much poorer general agreement between the calculated and observed multiplicities. In particular, the ^{1}H multiplicities are seriously overestimated while the ^{2}H and ^{3}H multiplicities are seriously underestimated.

In this assumption, the N/Z ratios of the residues in the simulated events follow the

valley of stability line in agreement with the supposition made on the detected fragment masses for the experimental events.

Based on the comparisons presented in figure 12, the hypothesis that appears to be the most reasonable is that which assumes that the source breaks into fragments which are characterized by the N/Z ratio of the initial system. This result reinforces the observation made with the EES calculations which predict that during the expansion phase from ρ_o to $1/3\ \rho_o$, the N/Z ratio of the expanding source remains equal to that of the entrance channel [2].

B. Mean kinetic energies

In figure 13, we compare the experimentally derived relative kinetic energies to the predictions of the GEMINI calculation when the primary fragments have the same N/Z ratio as the initial system. For neutrons and charged particles, these kinetic energies were calculated the same way as for the charged particles in the experimental data, i.e. relative to the residues ($E_{rel} = 0.5\ A\ V_{rel}^2$). For ^1H, and neutrons the mean kinetic energies deduced from the experiment are well reproduced by the calculation. For other emitted particles, the calculated energies are lower than the experimental ones. Maxwellian fits to the spectra calculated with a level density parameter of A/10, lead to apparent temperatures near 4 MeV regardless of the identity of the particle. The apparent temperatures derived from the experiment show a wider variation (figure 9, paragraph IV.B). The larger energies and temperatures that we observed experimentally might be explained by the fact that in the experimental events, the particles are subject to the Coulomb interaction with a large number of other fragments or light species which are also produced during the source disintegration. This complex environment is not taken into account in the GEMINI simulations. In order to verify whether this scenario can explain the discrepancies between the simulations with GEMINI and the experimental data, we performed calculations with the SIMON event

22

generator. In this generator, the interactions between the reaction products are taken into account in order to calculate the trajectory and kinetic energy of each particle. For the simulations with SIMON, the average excitation energy of the primary fragments was set to 2.8 MeV/nucleon. The kinetic energy spectra of the secondary light charged particles obtained with SIMON were slightly harder than the spectra calculated with GEMINI, but this difference was not sufficient to reproduce the experimental values. Therefore, we believe that the discrepancies between the data and the simulations should be attributed to the uncertainty in the background definition whose shape has been extracted from the proton emission simulations. This background shape might not approximate the background shapes of the other light particles, as well as for protons. This uncertainty has a noticeable effect on the kinetic energies because this quantity depends strongly on the shape of the background. On the contrary, for the extraction of the light charged particle multiplicities, the most important parameter is the depth of the background. For these reasons, the kinetic energies are much more affected by the uncertainty in the background shape than are the light charged particle multiplicities.

In order to estimate the effect of the kinetic energy uncertainties on the extraction of the total excitation energies of the primary fragments, we calculated this last quantity by replacing the experimental light charged particle kinetic energies by the kinetic energies given by GEMINI, without changing the experimental secondary multiplicities. As in section IV D., the neutron kinetic energies were again deduced from the proton kinetic energies. With the simulated kinetic energies, we obtained an average value of 2.85 MeV/nucleon for the primary fragment excitation energy. This quantity is very close to the value deduced from the experimental observables (3.0 MeV/nucleon). This reflects the fact that the Q value, which accounts for 55 % of the total excitation energy, is unchanged because the secondary multiplicities remain the same for both calculations. Further, since the GEMINI calculations reproduce well the experimental proton kinetic energies, the neutron kinetic energies deduced from the simulations are very similar to the values deduced from the experiment. Since the secondary neutron multiplicities are very high in comparison to the secondary light

23

charged particle multiplicities, the neutron kinetic energies are the dominant factor for the calculation of the total kinetic energy in formula 7. Therefore the differences observed in figure 13 between the calculated and experimentally observed kinetic energies do not lead to a significant change in the derived excitation energies.

VI. CONCLUSION

In conclusion, for the 50 MeV/nucleon ^{129}Xe+^{nat}Sn central collisions, with the help of light charged particle-fragments correlations, we have extracted the multiplicities of particles resulting from evaporation decay of the primary hot fragments. We have also extracted the relative kinetic energy distributions between the primary fragments and the light charged particles that they evaporate. We then reconstructed the average atomic numbers, masses and excitation energies of those primary fragments. From the comparison between the predictions of the GEMINI model with the experimentally observed secondary multiplicities of the evaporated light charged particles, we concluded that the primary excited fragments have the same N/Z ratio as the initial system ^{129}Xe + ^{nat}Sn. We reconstructed their initial excitation energies per nucleon and we noted that those last are very similar from one fragment to another and correspond to a mean value of 3.0 MeV/nucleon. It is interesting to note that this excitation energy per nucleon suggests primary fragment temperatures near 4.9 MeV, assuming a fermi gas level density parameter a=A/8. Such values are very close to those derived from the state ratio measurements [21–25]. This work proves that the primary fragments produced in the multifragmentation process are excited. The estimation of this internal fragment excitation energy, which corresponds to a 5 MeV temperature, seems to be consistent with a limiting temperature below which primary fragments deexcite only through evaporation.

The fact that the excitation energy of the hot multifragmenting source is shared between the fragments in the ratio of their masses, suggests that, on the average, thermodynamical equilibrium has been achieved at the disassembly stage of the source.

24

VII. ACKNOWLEDGMENTS

REFERENCES

[1] N. Marie et al., Phys. Lett. B **391**, 15 (1997).

[2] R. Bougault et al., proceedings of the XXXV Intern. Winter Meeting on Nuclear Physics (Bormio, February 1997), ed. I. Iori, page 251, LPCC97-04.

[3] A. Le Fevre, Thèse de Docteur en sciences de l'Université Paris 7.

[4] N. Marie, Thèse de Docteur en sciences de l'Université de Caen.

[5] A.S. Botvina, A.S. Iljinov, I.N. Mishustin, J.P. Bondorf, R. Donangelo and K. Sneppen, Nucl. Phys. **A475**, 663 (1987).

[6] J.P. Bondorf, A.S. Botvina, A.S. Iljinov, I.N. Mishustin and K. Sneppen, Phys. Rep. **257**, 133 (1995).

[7] J.P. Bondorf, A.S. Botvina, I.N. Mishustin and S.R. Souza, Phys. Rev. Lett. **73**, 628 (1994).

[8] W.A. Friedman, Phys. Rev. C **42**, 667 (1990).

[9] A. Bonasera, F. Gulminelli and J. Molitoris, Phys. Rep. **243**, 1 (1994).

[10] J. Pouthas et al., NIM A **357**, 418 (1995).

[11] J.C. Steckmeyer et al., NIM A **361**, 472 (1995).

[12] J. Pouthas et al., NIM A **369**, 222 (1996).

[13] J.F Lecolley et al., Phys. Lett. B **325**, 317 (1994).

[14] T.K. Nayak et al., Phys. Rev. C **45**, 132 (1992), and references contained therein.

[15] O. Lopez et al., Phys. Lett. B **315**, 34 (1993).

[16] Data extracted using NNDC On-Line Data Service from the ENSDF database, file revised as of 8 July 1996. M.R. Bhat, Evaluated Nuclear Structure Data File (ENSDF),

Nuclear Data for Science and Technology, page 817, edited by S.M. Qaim (Springer-Verlag, Berlin, Germany,1992).

[17] G. Bizard, private communication, LPC Caen.

[18] L. C. Vaz, J.M. Alexander, Z. Phys. A- Atoms and Nuclei **318**, 231-237 (1984).

[19] Seeger et Prisho, Los Alamos Report LA-3751 1967.

[20] R.J. Charity et al., Nucl. Phys. **A483**, 371 (1988).

[21] R. Wada et al., Phys. Rev. C **55**, 227 (1997).

[22] J. Pochodzalla et al., Phys. Rev. Lett. **75**, 1040 (1995).

[23] J.A. Hauger et al., Phys. Rev. Lett. **77**, 235 (1996).

[24] M.B. Tsang et al., Phys. Rev. C **53**, R1057 (1996).

[25] M. Assenard et al., Proceedings of the XXXV Intern. Winter Meeting on Nuclear Physics (Bormio, February 1997), ed. I. Iori, page 465.

FIGURES

FIG. 1. $V_{\parallel}^{IMF} - V_t^{IMF}$ diagrams obtained for alpha particles detected in coincidence with B, Ne, P and Ca fragments in experimental events (see text).

FIG. 2. Relative velocity spectra between Neon and alpha particles (left plot), Sulphur and proton particles (right plot) for correlated (continuous histograms) and uncorrelated (dashed histograms) experimental events.

FIG. 3. For simulations : Top) Relative velocity spectra for protons emitted in coincidence with Ne or Li correlated events. The total spectra (continuous histograms) and the spectra for the three separate components are shown. The dot-dashed histograms show the contribution from primary emission (see text). The hatched-dashed and dotted histograms show respectively the contributions from de-excitation of the primary fragments which produce and do not produce the considered fragments. (a) For correlated events and Ne fragments. (b) For uncorrelated events, but for protons detected in coincidence with Li whose velocities are replaced by Ne velocities (see text). (c) The correlation function (continuous histogram) for Ne-^{1}H. The associated real background (dashed histogram) and the contribution from secondary emission from the parents of the Ne fragments (hatched area) are also shown. (d) The difference function (continuous histograms) for Ne-^{1}H. The associated real background (dashed histogram) and the contribution from secondary emission from the parents of the Ne fragments (hatched area) are also shown. (e) and (f) Same as (c) and (d) except that the dashed histograms represent the backgrounds derived according to the method described in the text.

FIG. 4. Difference functions and correlation functions for hydrogen isotopes detected in experimental events and correlated with various fragments : 4(a) to 4(f) Difference functions (continuous histograms) and their associated calculated backgrounds (dashed histograms). 4(g) to 4(l) Correlation functions (continuous histograms) and their associated calculated backgrounds (dashed histograms). 4(m) to 4(r) Secondary evaporated spectra.

28

FIG. 5. Same as figure 4 for helium isotopes detected in experimental events and correlated with various fragments.

FIG. 6. For experimental events, average secondary multiplicities per IMF, $< M >$, of the evaporated hydrogen and helium isotopes, as a function of the detected IMF atomic number Z_{IMF}.

FIG. 7. Average relative kinetic energies between the primary fragments and the evaporated hydrogen and helium isotopes, as a function of the detected IMF atomic number, Z_{IMF}.

FIG. 8. Values of the parameters E_B obtained for the fit of the relative kinetic energy spectra of the hydrogen and helium isotopes, as a function of the detected IMF atomic number, Z_{IMF} (see text).

FIG. 9. Values of the parameters T obtained for the fit of the relative kinetic energy spectra of the hydrogen and helium isotopes, as a function of the detected IMF atomic number, Z_{IMF} (see text). For each light particle, the dotted line represents the mean value of the temperatures, calculated over the fragment atomic number range considered.

FIG. 10. (a) Average atomic number of the primary fragments, Z_{pr}, as a function of the detected IMF atomic number Z_{IMF}. (b) Average masses of the primary fragments, A_{pr}, as a function of the detected IMF mass A_{IMF}. The triangles correspond to the case where the primary fragments are in the valley of stability. The squares represent the case where the primary fragments have the same N/Z ratio as the combined system $^{129}Xe+^{nat}Sn$.

FIG. 11. Average total excitation energies of the primary fragments, as a function of their atomic number, Z_{pr}. The experimental results are represented with black circles and the GEMINI calculations performed for different compound nucleus excitation energies are symbolized by open symbols. (a) The initial fragments have the same N/Z as the combined system. (b) The masses A_{pr} of the initial fragments were estimated assuming they are in the valley of stability.

FIG. 12. Comparison between the multiplicities of neutrons and light particles predicted by GEMINI to the experimentally observed multiplicities of hydrogen and helium isotopes (black circles) and to the neutron multiplicities estimated when we assume that the primary fragments conserve the N/Z ratio of the entrance channel (black triangles), as a function of the residue atomic number. The open symbols correspond to the assumption of neutron rich compound nuclei. The lines represent the case in which the compound nuclei are in the valley of stability.

FIG. 13. Relative kinetic energies of the light charged particles and neutrons, as a function of the residue atomic number, resulting from the experimental data (black symbols) and predicted by the GEMINI model when the primary fragments have the same N/Z ratio as the initial system (open symbols).

TABLE I. Average multiplicities of light charged particles, intermediate mass fragments and fragments of various atomic numbers accounted for the isotropic source, for events characterized by $45° \leq \theta_f \leq 60°$ (left column), and for events characterized by $\theta_f \geq 60°$ (right column). The numbers in brackets represent the statistical errors.

Isotope	M_{iso}	M_{iso}
	$45° \leq \theta_f \leq 60°$	$60° \leq \theta_f$
^{1}H	6.81 (0.01)	6.94 (0.01)
^{2}H	3.90 (0.01)	3.94 (0.01)
^{3}H	2.74 (0.01)	2.76 (0.01)
^{4}He	7.15 (0.01)	7.30 (0.01)
^{3}He	0.88 (0.01)	0.91 (0.01)
IMF	7.10 (0.01)	7.10 (0.01)
Li	1.58 (0.01)	1.58 (0.01)
Ne	0.30 (0.01)	0.30 (0.01)
S	0.097 (0.002)	0.094 (0.002)

TABLE II. Average kinetic energies of Z=1 and Z=2 isotopes, Li, Ne and S fragments associated to the isotropic source, for $45° \leq \theta_f \leq 60°$ (left column), and for $\theta_f \geq 60°$ (right column). The numbers in brackets represent the statistical errors.

Isotope	E (MeV) $45° \leq \theta_f \leq 60°$	E (MeV) $60° \leq \theta_f$
^{1}H	25.9 (0.08)	26.0 (0.08)
^{2}H	32.5 (0.12)	33.0 (0.13)
^{3}H	31.9 (0.15)	32.2 (0.15)
^{4}He	32.7 (0.09)	32.9 (0.09)
^{3}He	49.5 (0.33)	49.4 (0.34)
Li	56.4 (0.31)	58.9 (0.32)
Ne	84.2 (1.02)	91.9 (1.02)
S	99.7 (2.42)	105.2 (2.36)

TABLE III. Multiplicities per event of the secondary particles evaporated by the primary fragments, M_s, multiplicities per event of light charged particles emitted by the isotropic source, M_{iso}. P is the percentage of M_s in comparison with M_{iso}.

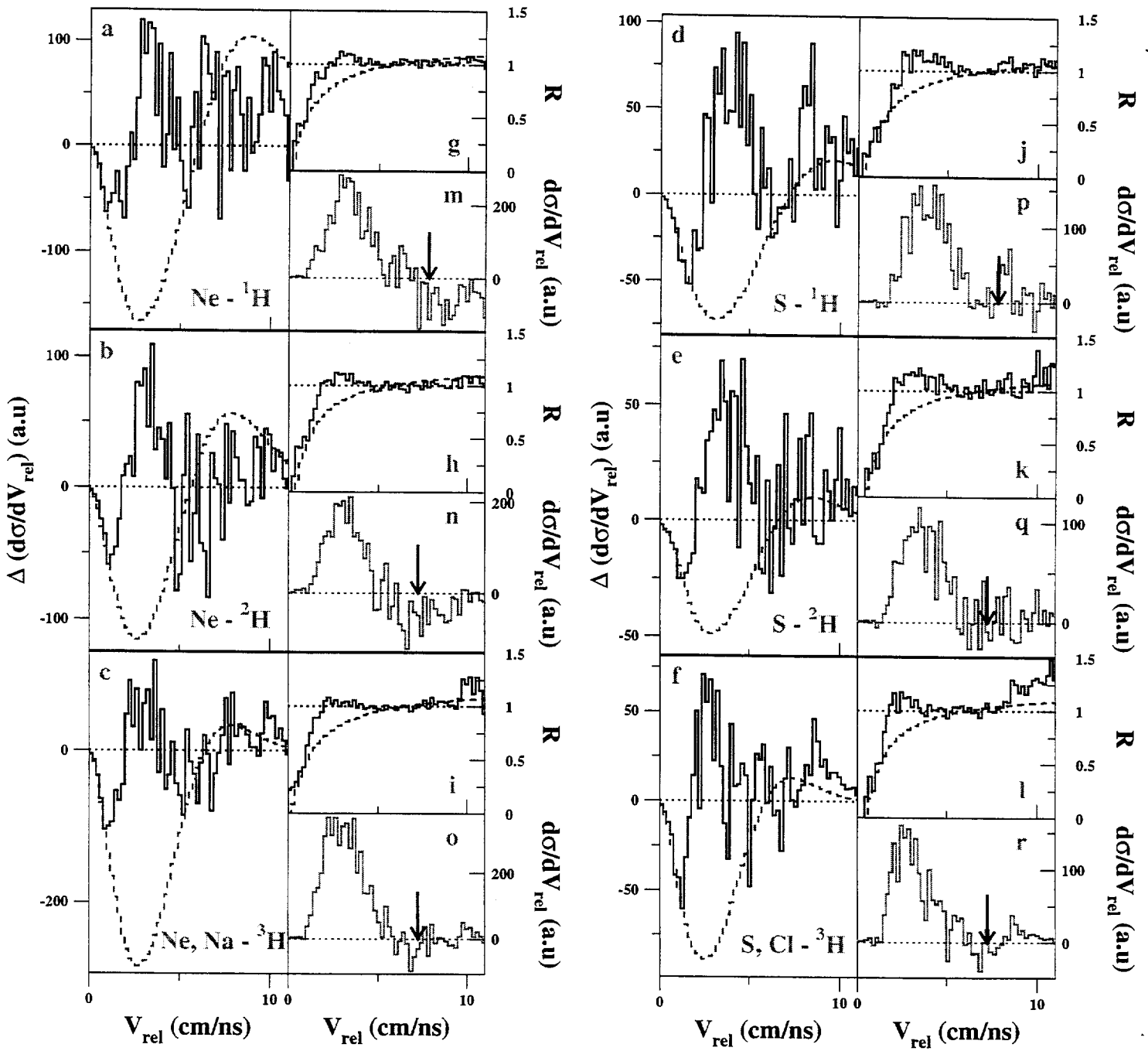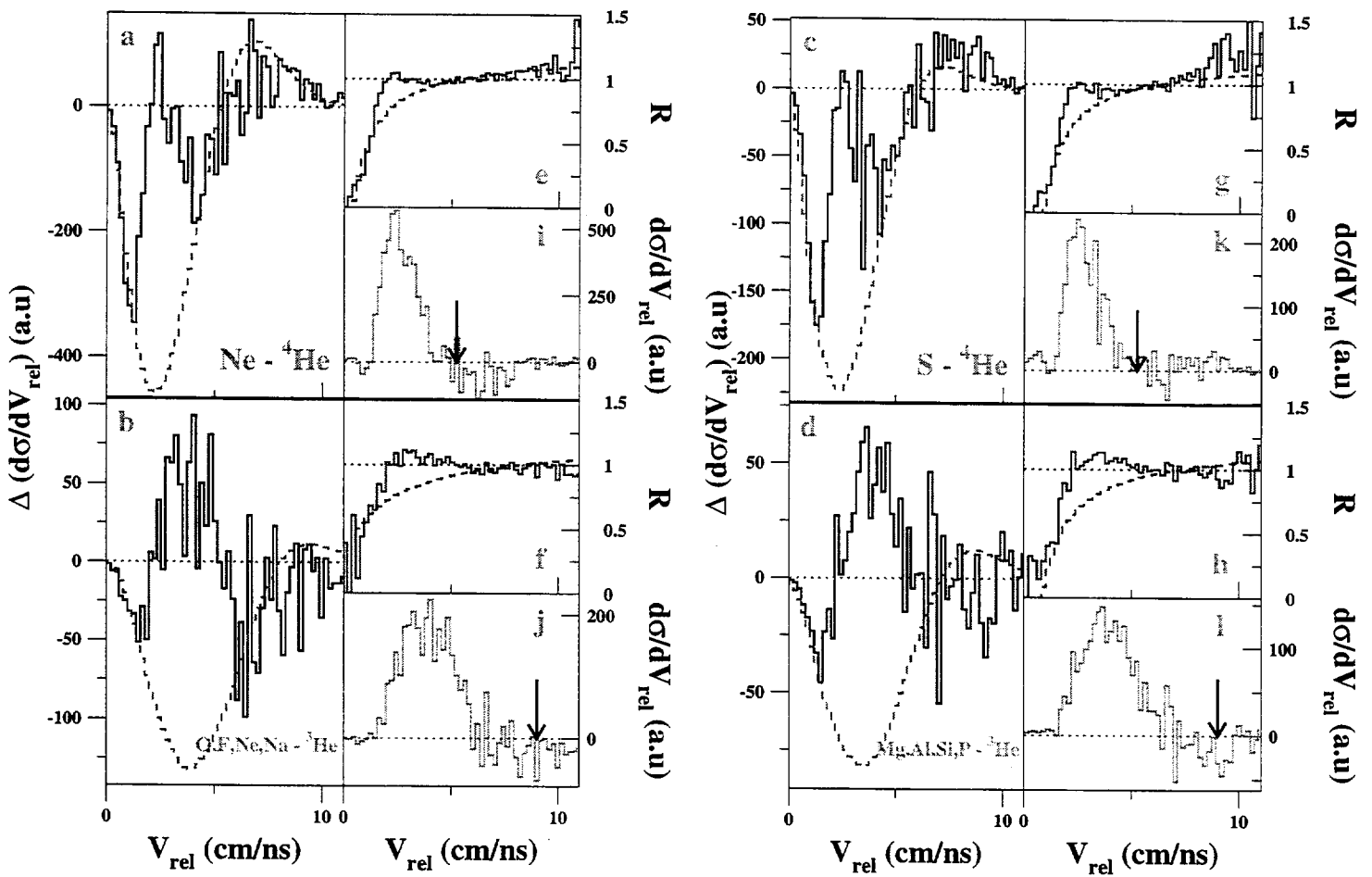| Isotope	M_s	M_{iso}	$P = M_s/M_{iso}$ (%)
^{1}H	$1.4^{+0.12\,(8.6\%)}_{-0.35\,(25\%)}$	6.87	$20.4^{+1.7}_{-5.1}$
^{2}H	$1.2^{+0.32\,(26.7\%)}_{-0.25\,(20.8\%)}$	3.92	$30.6^{+8.2}_{-6.4}$
^{3}H	$0.8^{+0.14\,(17.5\%)}_{-0.11\,(13.8\%)}$	2.75	$29.1^{+5.1}_{-4}$
^{4}He	$2.2^{+0.43\,(19.5\%)}_{-0.29\,(13.2\%)}$	7.2	30.5^{+6}_{-4}
^{3}He	$0.34^{+0.13\,(38.2\%)}_{-0.05\,(14.7\%)}$	0.88	$38.6^{+14.8}_{-5.7}$
total	$6.03^{+1.14\,(18.9\%)}_{-1.05\,(17.4\%)}$	21.62	$27.9^{+5.3}_{-4.8}$

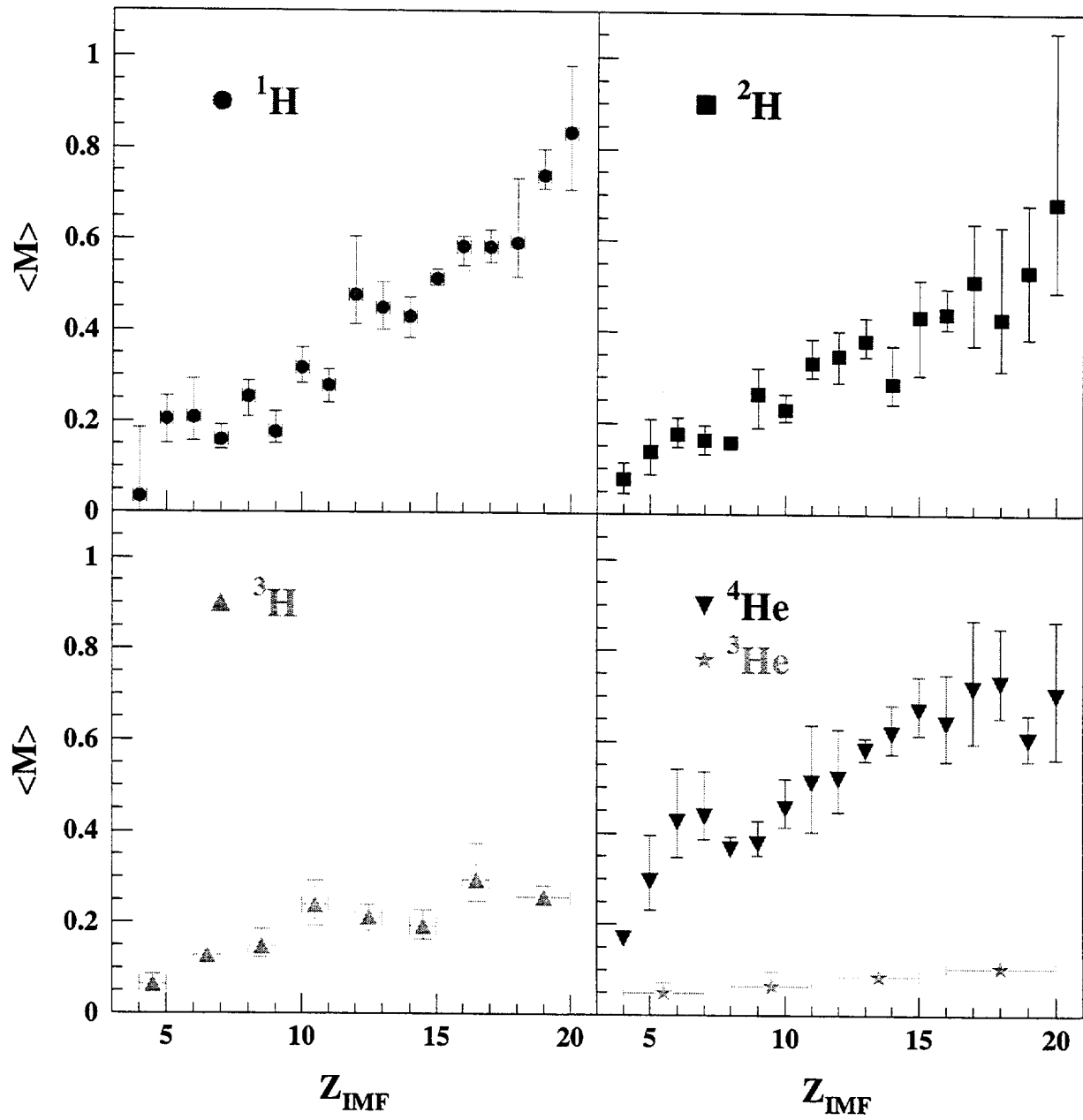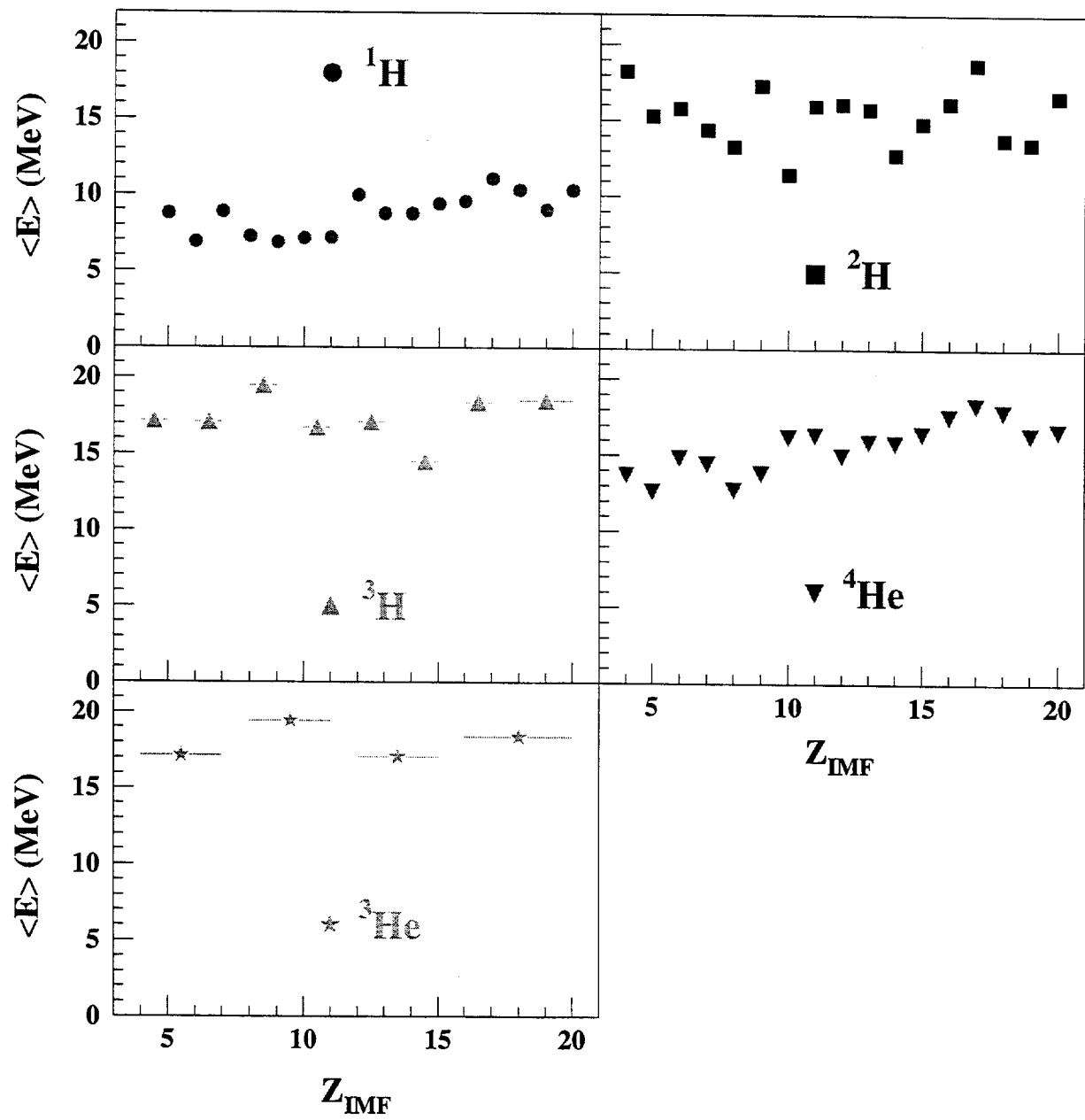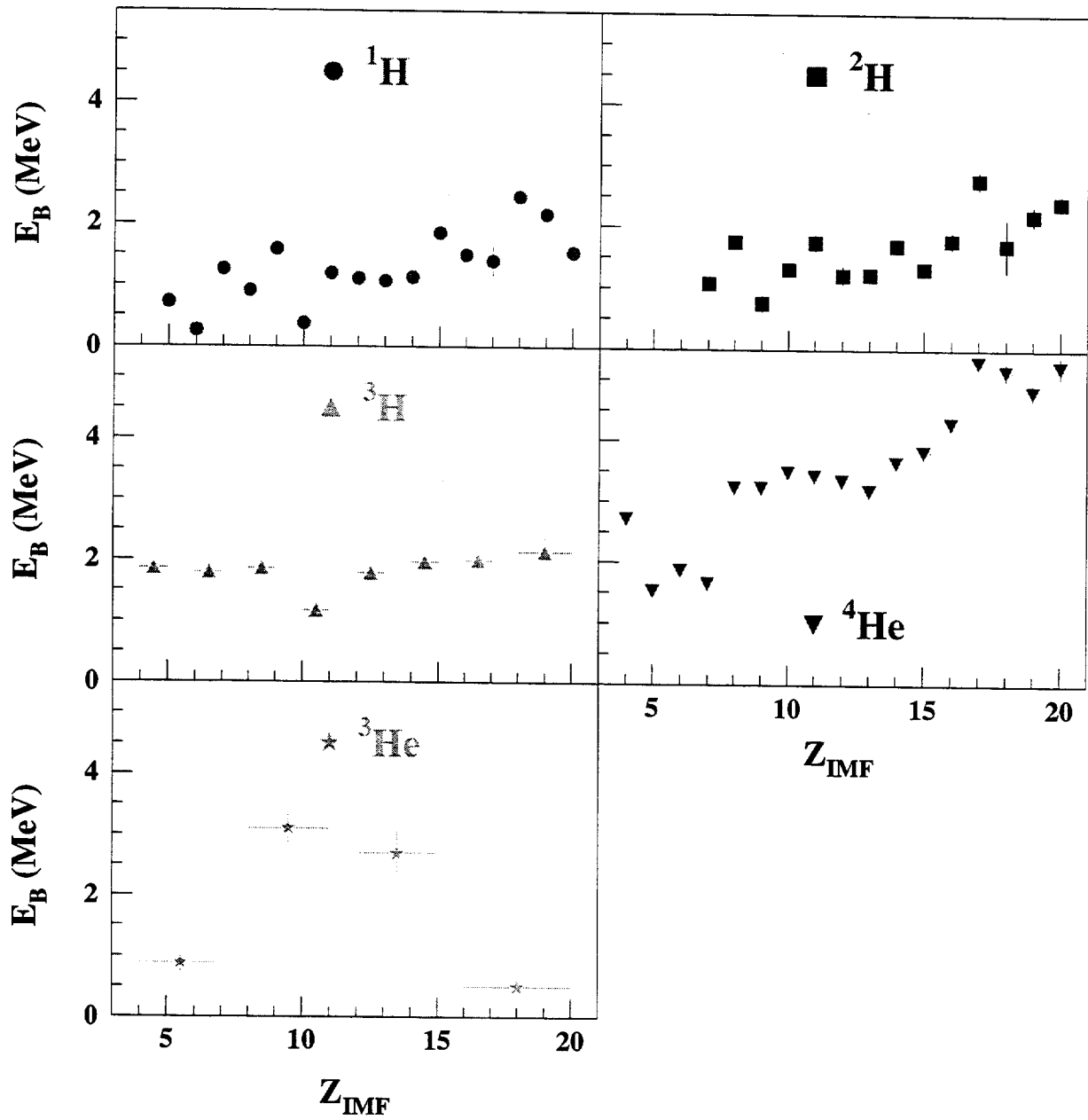^{129}Xe + ^{nat}Sn 50 A MeV, Alphas
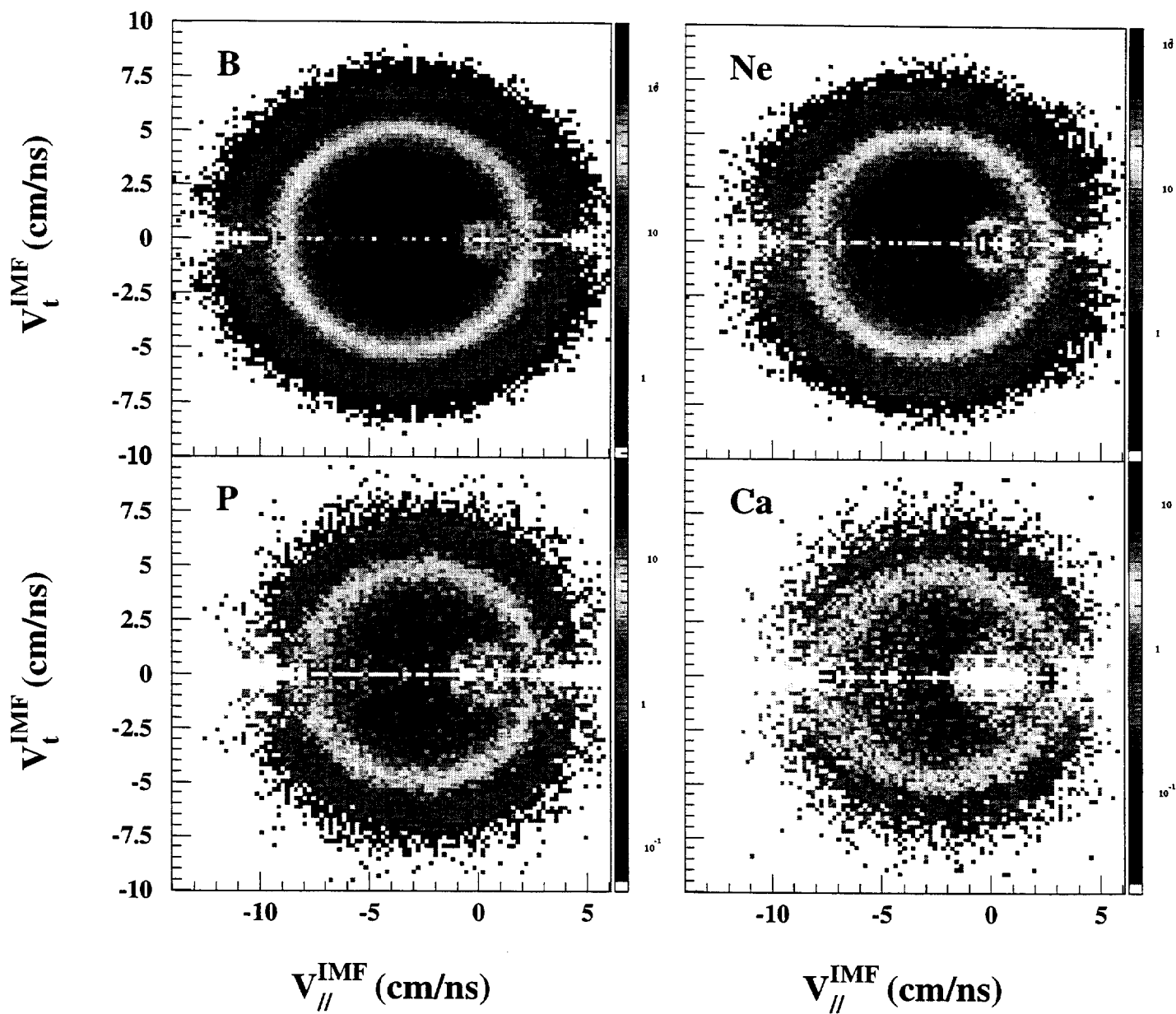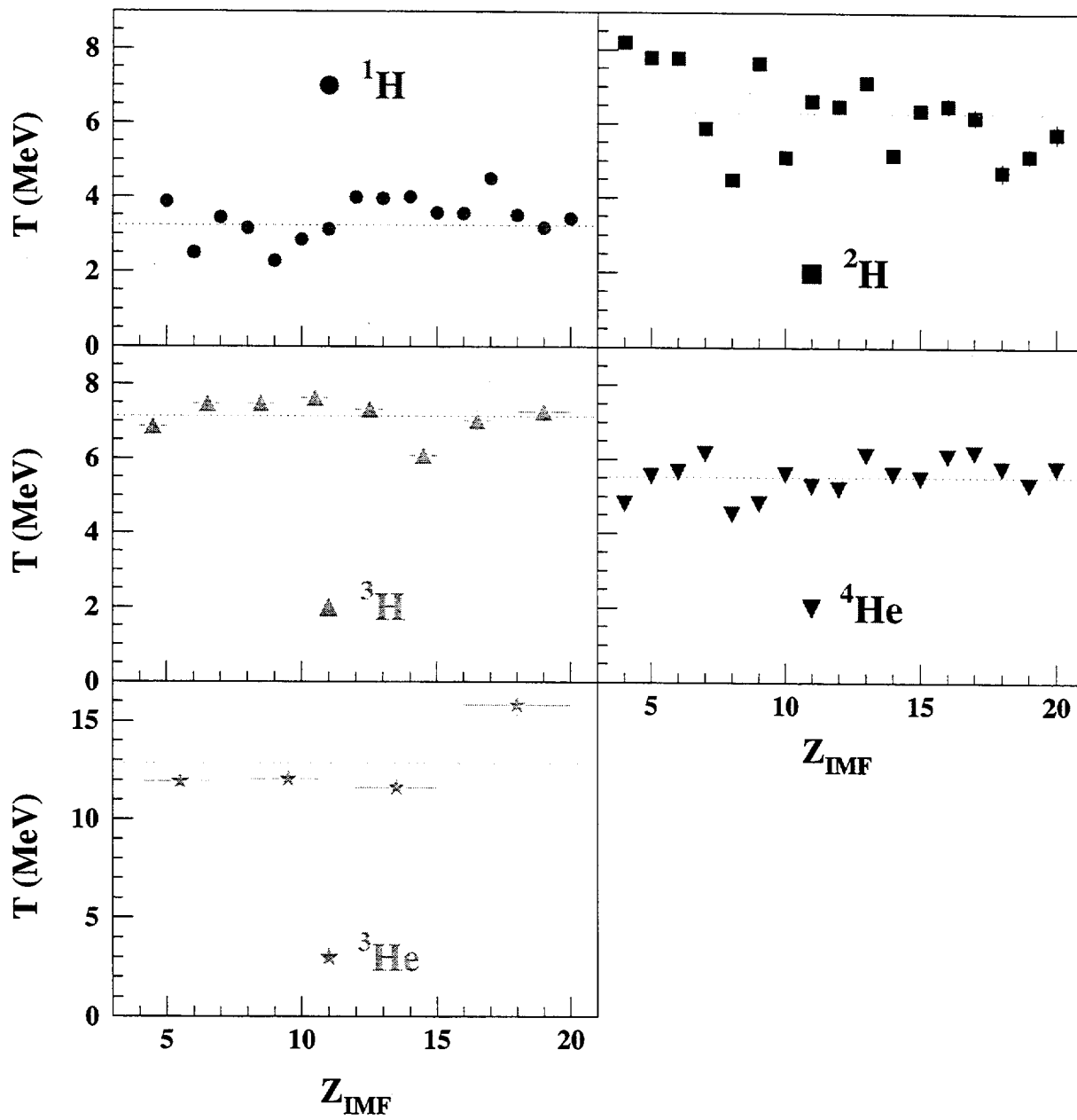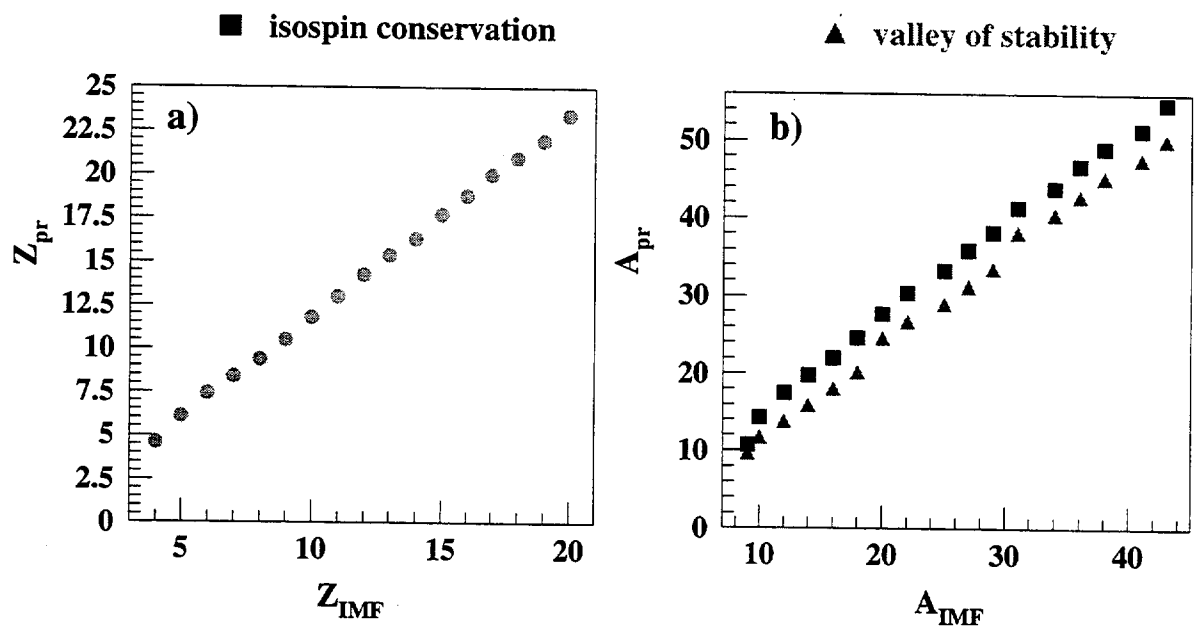
Fig. 1
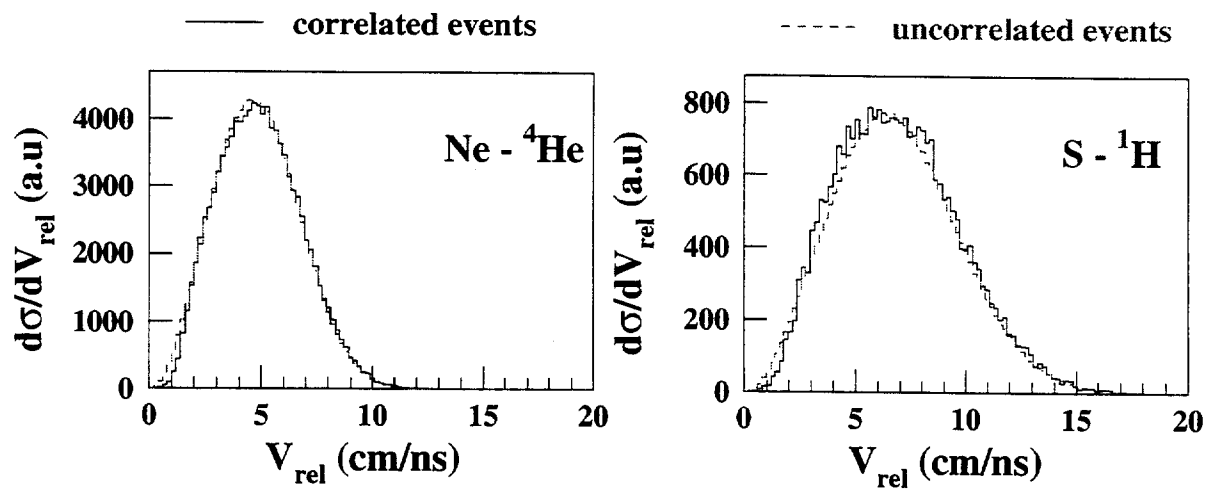
Fig. 2
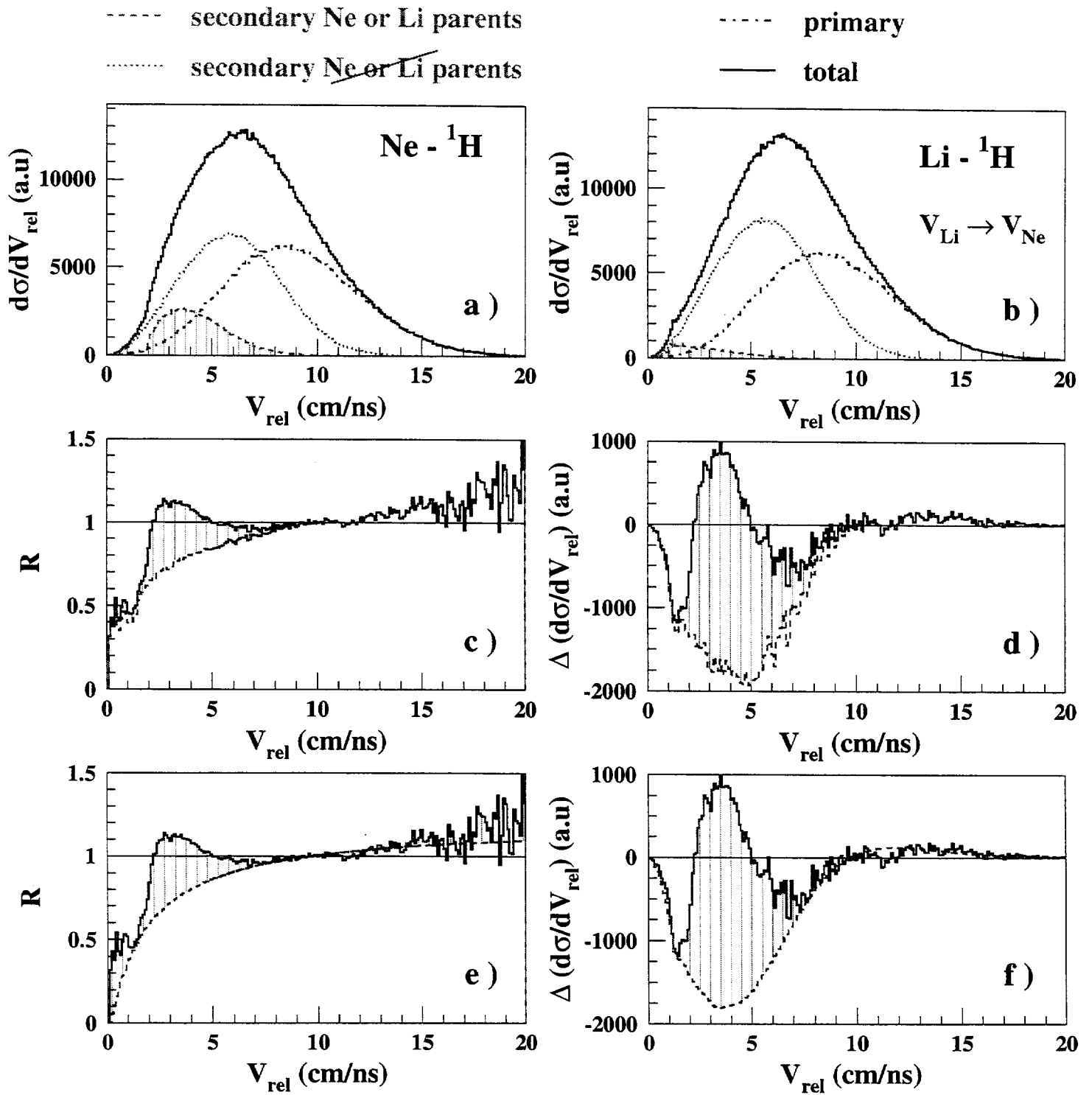
Fig. 3

Fig. 4

Fig. 5

Fig. 6

Fig. 7

Fig. 8

Fig. 9

Fig. 10

Fig. 11

Fig. 12

Fig. 13